

EXPERIMENTAL CHARACTERIZATION OF A ROBOTIC INFLATABLE WHEEL

Dimitrios Apostolopoulos⁽¹⁾, Michael D. Wagner⁽¹⁾, Chris Leger⁽²⁾, Jack Jones⁽²⁾

⁽¹⁾The Robotics Institute, Carnegie Mellon University, Pittsburgh, PA 15213, USA, Email: {davl,mwagner}@ri.cmu.edu

⁽²⁾Jet Propulsion Laboratory, 4800 Oak Grove Drive, Pasadena, CA 91109, USA, Email: {chris.leger,jack.a.jones}@jpl.nasa.gov

ABSTRACT

Inflatable wheels are a promising concept for long-range exploration of Mars as well as extremely rugged terrestrial terrains. This paper describes experimental studies that characterize the mobility of a single robotic inflatable wheel in terms of its ability to negotiate Mars-like cohesion-less soils, climb large discrete obstacles and endure the wear and tear caused by driving over kilometers of abrasive rocks. These studies were performed with a testbed apparatus that allowed variation of tire design, wheel loading, speed / acceleration profiles, tire pressure and traverse length. An in-line brushless motor controlled by a PID velocity control loop drives the wheel. This paper summarizes the most significant experimental results and discusses the impact of those results on aspects of robotic vehicles with inflatable wheels, such as state estimation and motion control.

Keywords – inflatable wheel, inflatable robotic rover, robotic mobility, motion control, robot design, space robotics

1. GENERAL SPECIFICATIONS

Inflatable robotic rovers (IRR) are a promising concept for long-range exploration and access to high-risk areas on planetary surfaces [1]. Through inflation or expansion of their locomotion elements, inflatable rovers can achieve extraordinary terrainability not possible by other conventional mobility systems while maintaining respectable travel speeds. Inflatable rovers such as JPL's prototype shown in Fig. 1 can drive over extreme terrain and surmount obstacles with ease. This is a distinct advantage over fixed wheel size configurations, which are forced to drive around obstacles. The effect of large diameter inflatable wheels on the performance of a rover is paramount. For example, a rover with drive wheels 1.5 m in diameter



Fig. 1: JPL's inflatable rover prototype during field testing (Courtesy: JPL)

would theoretically surmount 90% of discrete obstacles on the Martian surface [2], [3], [4]. Because of low stowage requirements, inflatable rovers offer an advantageous solution for maximizing space rover performance while satisfying fixed mass and volume constraints.

This new class of vehicle represents a departure from typical rovers with small, rigid tires. The inflatable tires flex and envelop obstacles and may not maintain a nominal wheel radius [5]. These departures lead to questions of how this type of vehicle should be controlled. For instance, what are the costs of obstacle climbing? Is dead reckoning possible? We will explore these questions using results from inflatable wheel mobility tests carried out in a wheel testbed constructed at Carnegie Mellon.

2. EXPERIMENTAL SETUP

Our IRR testbed consists of an inflatable wheel carried on a support structure capable of carrying the wheel and axle assembly across a test surface in a straight line. The test surface consists of a 10 m x 2 m sandbox in which various materials can be placed such as sand, rocks and obstacles. A brushless DC motor drives the wheel along with motion control hardware and various sensors placed on the testbed [6].

A pivoted frame structure was placed around the wheel. Both ends of the wheel axle are attached to the frame (see Fig. 2). The frame allows significant vertical motion of the wheel as it climbs over obstacles,

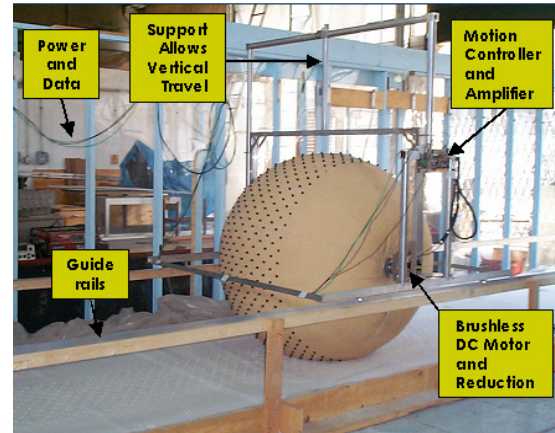


Fig. 2: CMU's inflatable wheel testbed

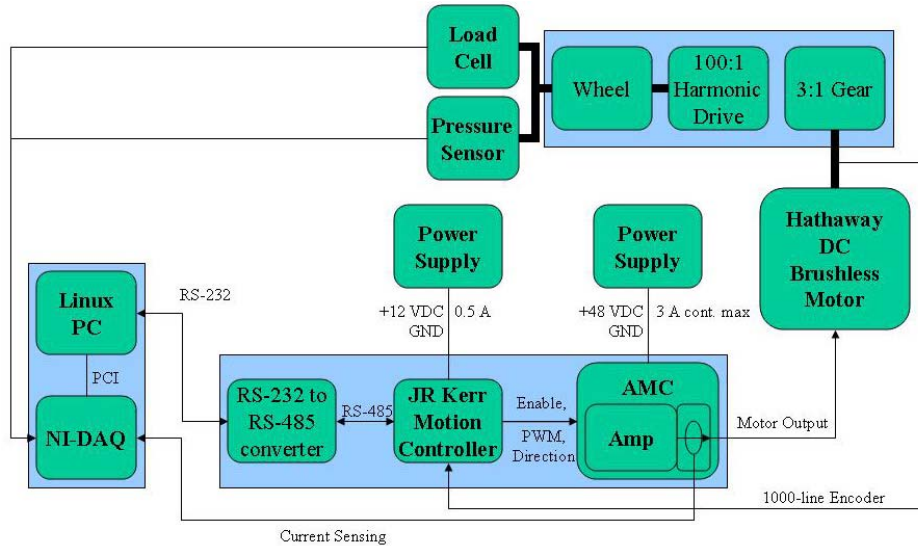


Fig. 3: Testbed electronics layout

and rides on guide rails to allow motion back and forth in the sandbox. Weights can be attached to the frame and aligned so that the force of weight on the wheel is evenly distributed on both axle attachment points. A motion controller, motor amplifier and other electronics are also mounted on the frame. Cabling provides power to the testbed and links it with a control station nearby.

The wheel is driven by a brushless motor coupled to the axle via a gearbox and harmonic drive with an overall reduction ratio of 300:1. The motor is driven by a brushless amplifier and a 300-watt, 48 VDC power supply.

The testbed allows the control of wheel angular velocity (rad/s) and acceleration (rad/s²). Users specify velocity and acceleration commands on a control station PC through a graphical user interface. The GUI sends commands via TCP/IP to a testbed server process, which in turn communicates via RS-232 to a JR Kerr PIC-Servo motion controller. The motion controller drives the amplifier with PWM output and maintains a desired velocity with a PID control loop based on feedback from a 1000-line encoder.

The testbed has been instrumented with load cell and pressure transducers to measure external loading and tire inflation, respectively. Measurements of the drive motor's current combined with measurements of the wheel's rolling radius will be combined to compute drive torque and power. The testbed electronic components are organized as shown in Fig. 3. A server process collects data from several sources at approximately 10 Hz (not real-time), which are then organized into a time-stamped, Matlab-compatible log file. Wheel loading is another important variable for

these tests. The cumulative weight of the wheel, axle and frame was measured by driving the wheel onto a digital scale and recording manually the result. The digital scale is accurate to 0.01 kg.

3. MOBILITY RESULTS

3.1 Contact Patch

The wheel's contact patch was measured by lowering the treaded tire alone into the sandbox and measuring the wheel loading, its contact patch, its sinkage and the inner tube inflation pressure. The treaded wheel mass was about 7.5 kg. At this loading, the contact patch was a circle approximately 1300 cm² in area. On average, the tire sank only a few millimeters into the sand. The inflation pressure at this loading was approximately 0.09 psi.

3.2 Rolling Resistance

Flat terrain tests are useful to measure the coefficient of rolling resistance. The coefficient of rolling resistance was calculated with the following formula:

$$C_{RR} = T i \text{ gear_ratio} / F_w / r \quad (1)$$

Where CRR is the coefficient of rolling resistance, T is the drive motor's torque constant in Nm/A, i is the current to the drive motor, gear_ratio is the gear ratio between motor and wheel, F_w is the weight of the wheel in N and r is the radius of the wheels' compressed axis in meters.

We performed two tests consisting of driving over flat terrain. For both tests, the mass of the wheel was approximately 15.2 kg and the wheel radius measured

along the compressed axis was about 70 cm. One test used a treaded tire (see the tire in Fig. 2) and one used a smooth tire made of the same material but without the rubber cleats. The results of these tests showed that the coefficient of rolling resistance between both tires and the soil is between 0.10 and 0.15. Over these tests, the smooth tire sees a mean rolling resistance of 13% of the vertical loading at the contact patch and the treaded tire sees a nearly identical mean rolling resistance of 11% of the vertical loading at the contact patch.

In both cases, the rolling resistance increases over time as the wheel traverses the testbed. This consistently occurs as the wheel drives in either direction, so the effect cannot be due to a sloped testbed track. Simplistically, a sloped track would result in a trend similar to that shown as a dotted black line in Fig. 4. However, we observed trends similar to those shown in blue, with rolling resistances increasing from around 0.1 to around 0.18. An explanation to this phenomenon probably lies in the fact that the tire is very compliant. As the tire tries to overcome ground resistance force it deforms up to point at which it has gained enough

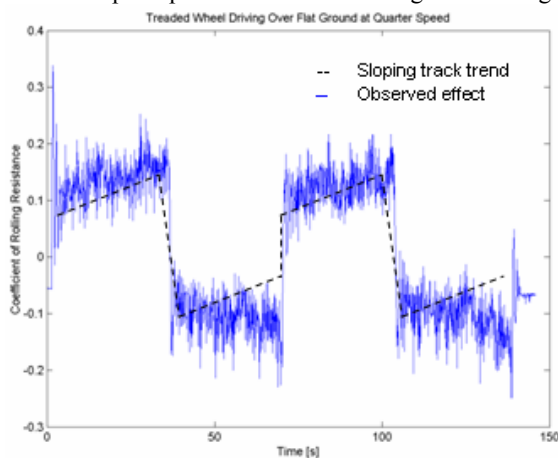


Fig. 4: Rolling resistance increases as the wheel travels on the track in either direction, which cannot be explained by a sloping track

structural rigidity to transmit the necessary torque to overcome the ground resistance and to produce forward motion. Moving forward mitigates the radial deformation of the tire which in turn causes the tire to tire to “demand” more torque to overcome the resistive ground forces.

3.3 Obstacle Climbing

3.3.1 Tread Design

Fig. 5 depicts the two types of tires climbing over a 20-cm obstacle. Both wheels were traveling at 0.13 rad/s. The mass of the treaded tire was 15.0 kg and the mass of the smooth tire was 14.3 kg. Both had compressed

wheel radii of about 70 cm. While climbing up the face of the obstacle, the treaded tire faced less obstacle resistance than the smooth tire. The maximum obstacle resistance coefficient of the treaded tire was 0.88 while the smooth tire’s maximum was 1.01. This change in resistance cannot be explained by the 0.7 kg wheel mass difference. Therefore the change quantifies the obstacle climbing benefits provided by the treaded tire. Note that resistance coefficients larger than 1.0 are due

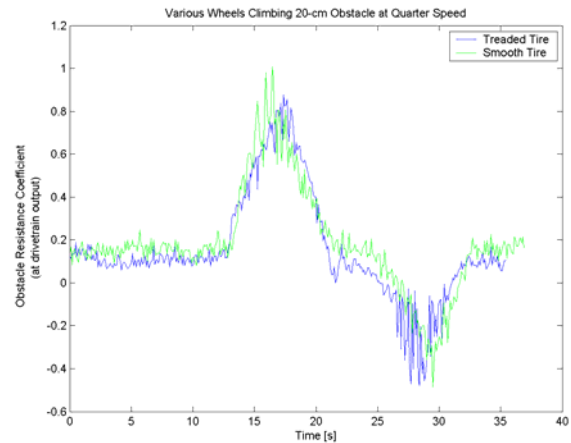


Fig. 5: The treaded tire sees a maximum 1.01 obstacle resistance coefficient while the smooth tire’s maximum is 0.88

to the ground and frictional losses internal to the frame.

The obstacle-climbing difficulties of a smooth tire are further shown in Fig. 6. Here we see the 70-cm radius smooth tire failing to climb a 40-cm discrete obstacle. About 29 seconds into the test, the wheel meets the front face of the obstacle and begins climbing it. At about 31 seconds, the wheel has not yet climbed the obstacle and begins to slip. This continues for another 7 seconds, at which time the test was cancelled because the wheel could not finish the climb. This test was repeated with similar results. Later in this paper we will see that the treaded tire can reliably climb the same 40-cm obstacle.

3.3.2 Wheel Loading

The first set of tests with the smooth tire involved driving over a 20-cm obstacle at an angular wheel velocity of 0.13 rad/s. One wheel had a mass of 14.3 kg, the other had a mass of 19.9 kg. Fig. 7 shows the interesting results. As the wheels climb the front face of the obstacle (marked with an “A”), the lighter wheel experiences a higher maximum obstacle resistance (1.01) than does the heavier wheel (0.82). This could be because the heavier wheel deforms more over the leading edge of the block. If the wheel deforms around the front face of an obstacle, it gains better climbing

ability. The part of Fig. 7 marked “B” depicts the wheels climbing down the far edge of the obstacle. In this case the motor’s current draw (and therefore calculated obstacle resistance coefficient) is negative as the motion controller overcomes the tendency of gravity to back drive the motor. The values here actually represent tractive effort, not obstacle resistance. This should be noted in all subsequent obstacle-climbing tests.

3.3.3 Obstacle Height

Fig. 8 shows the relationship between obstacle height and obstacle resistance coefficient. Both tests involved driving the treaded wheel at 0.13 rad/s angular velocity towards the obstacle. The blue plot represents the wheel driving over a 40-cm obstacle (two wooden blocks), while the green plot represents the wheel driving over a 20-cm obstacle (one wooden block).

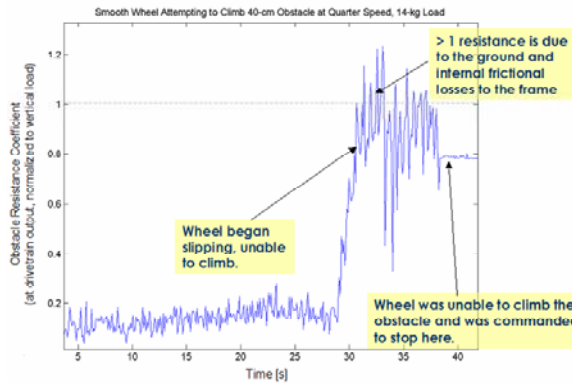


Fig. 6: The smooth tire repeatedly failed to climb a 40-cm obstacle

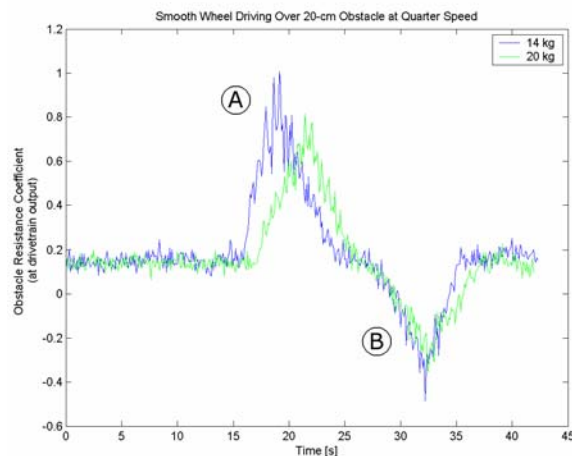


Fig. 7: When more weight is applied, the inflatable wheel experiences more deformation, actually decreasing the power to climb an obstacle

At the outset of both tests, the wheel began driving over the flat sand leading up to the obstacle. As we

would expect, both plots are similar in this region. The

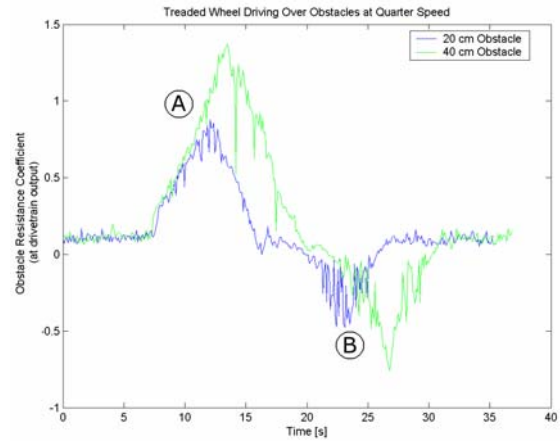


Fig. 8: The treaded tire driving over 20-cm and 40-cm obstacles

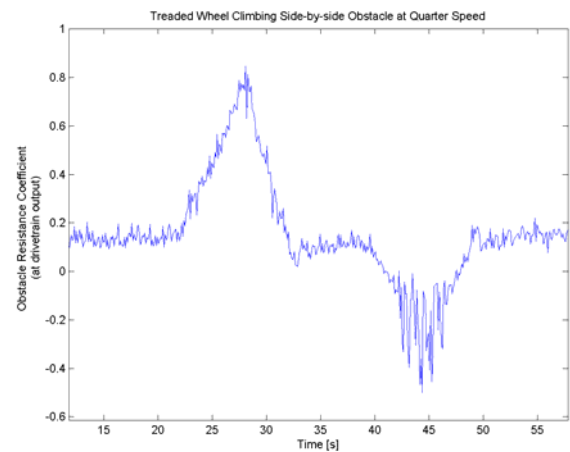


Fig. 9: The peak resistances show how long the wheel takes to finish climbing a discrete obstacle

plots then peak as the wheel pushes into the obstacle. If we look at the apex of these peaks (marked with an “A”) we see that the obstacle resistance reaches nearly 1.5 surmounting the 40-cm obstacle and nearly 1.0 surmounting the 20-cm obstacle. Note that the 40 cm obstacle took longer to surmount because the wheel had to slowly pull itself up the obstacle face. The tire’s studs and ability to deform easily helped the wheel drive over the higher obstacle. Further tests will better explore the limits of what size obstacles can be surmounted. A third region of the figure (marked “B”) shows the wheel scaling down the far face of the obstacle. Again, we see that more current (and therefore power) is required to control the motor as it drives down the higher obstacle.

3.3.4 Tire Deformation

We performed further tests that involved two wooden block obstacles side by side, so that the wheel would climb up one, travel on top of the two blocks and then climb back down. The treaded wheel was used with a 14.98 kg loading and driven at 0.13 rad/s angular velocity. The obstacle resistance coefficient is plotted in Fig. 9.

These tests give an idea of how quickly the motor's current draw rises and falls as the wheel climbs. Climbing up the front face (marked "A") takes approximately 6 seconds, which is expected given the angular velocity, obstacle height and wheel radius. In another 5 seconds the wheel has finished climbing and the motor current draw decreases back to a nominal flat driving level. Understanding the behavior as the wheel climbs down the obstacle (marked "B") is more difficult. An initial analysis shows that it takes approximately 11 seconds for the wheel to reach the threshold, climb down and return to nominal flat driving power levels. In particular, a great deal of oscillation occurs when the wheel falls back off the obstacle.

3.3.5 Drawbar Pull

The maximum drawbar pull capacity of the wheel was determined by measuring the maximum "trailer" force the wheel sustains at reasonable slippage (ideal value of 20%). The wheel was driven while its frame was attached to a fixed surface using a horizontal steel cable. A load cell mounted inline with the cable measures the horizontal drawbar pull force as the wheel tries to propel forward.

Each drawbar pull test consists of five operating regions. In region "A", the wheel driving away from the wall, extending the slack steel cable and still driving normally. In region "B" the cable tension rapidly increases and so the tire begins to deform. Deformation continues until region "C", where the wheel begins slipping and the cable remains taught. This continues until region "D" when the wheel is commanded to stop. The cable then begins to slack in region "E" and the wheel drives back towards the wall. Fig. 10 shows the force sensed by the load cell during three tests of the treaded tire. The treaded tire weighing in at 15 kg consistently achieves a drawbar pull of roughly 140 N just before it begins slipping. Fig. 11 shows the results of a 15-kg smooth tire. It achieved a drawbar pull of only 95 N.

The arc tangent of the ratio of drawbar pull to wheel loading is approximately equal to maximum gradeability that an IRR could achieve just before the soil that covers the slope fails [7]. This is a particularly useful result because it provides an empirical way of estimating the limit of gradeability independently of

the vehicle design and location of the center of gravity or torque / power capacity of its propulsion motors. By this measure, the treaded tire's theoretical gradeability on loose sand is roughly 43 degrees. In practice, that will not be attainable because a sandy slope of over 35 degrees is not stable.

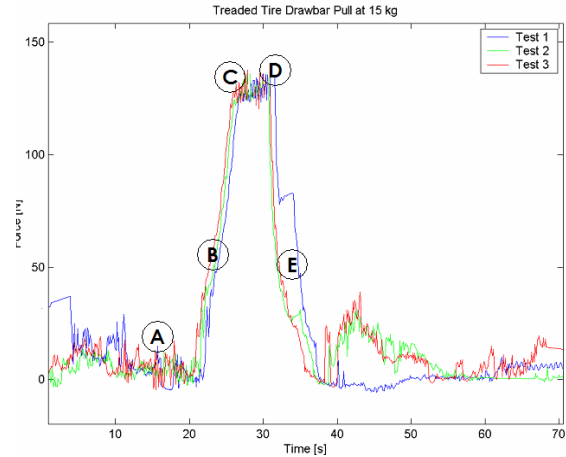


Fig. 10: The mean drawbar pull is 140 N across three tests with the 15-kg treaded tire

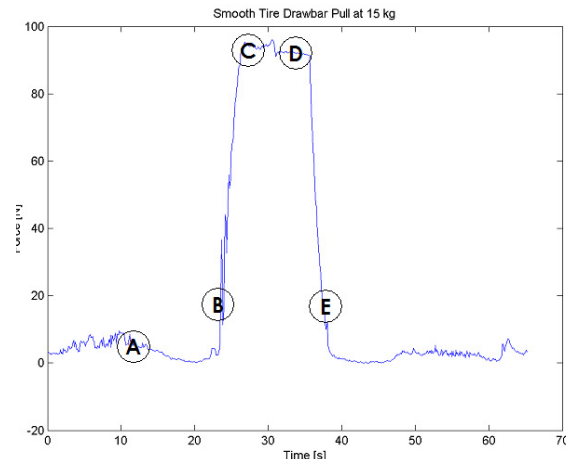


Fig. 11: The drawbar pull of the 15-kg smooth tire is 95 N

4. IMPLICATIONS TO INFLATABLE ROBOTIC ROVER DESIGN

4.1 Wheel Design

The results we collected strongly suggest that a treaded inflatable tire be used in IRR designs. The obstacle climbing ability of a smooth inflatable tire is too poor to justify its added complexities in vehicle control and mechanism deployment. However with cleats or treads, the wheel is capable of climbing large obstacles over half the wheel radius. Consistently the treaded tire

delivered 20% more traction and obstacle climbing ability than the smooth tire.

4.2 Control

An important result of this work is that a straightforward velocity PID controller was capable of driving the IRR wheel over obstacles that were over half the radius of the wheel. Oscillations that occur as the wheel bounces against and off of obstacles did not cause instabilities for the motion controller. Furthermore, no instabilities or failure modes were observed while performing long-duration “traverses” with an overall distance of 60 km.

4.3 Dead Reckoning

IRRs pose two challenges to dead reckoning. First, the compressed-axis wheel radius changes over time due to loading and dynamic effects. The extremely low inflation pressure posed problems when we attempted to correlate pressure, loading and compressed-axis wheel radius. Therefore, we suggest that this radius be sensed externally. Additionally, further development of tire material is needed to more fully seal the tire’s inner tube and avoid deflation.

Another challenge to dead reckoning with an IRR is wheel deformation while driving over obstacles. In this case, motion at the reduction output does not translate into actual wheel motion. Instead, the wheel itself is stretched. The effect is similar to slip, in that the encoders report movement but the vehicle is not moving. However, unlike typical soil slip, at some point the spring force is relieved and the vehicle moves forward without the encoder reporting movement. In other words, the assumption that predictable angular velocity-based motor control translates to predictable vehicle velocity is false.

While these limitations call out for inertial sensing to replace proprioception, the dynamics of an inflatable wheel may make inertial sensing very noisy, particularly at speeds above 1.5 m/s. More work on this need should be carried out in the future.

4.4 Obstacle Negotiation

As expected, a great deal of tire deformation is seen when climbing obstacles. This deformation was seen as beneficial in two ways. First, it results in a larger soil contact patch and therefore more traction than would be seen with a similarly sized rigid tire. Secondly, as the wheel climbs over obstacles it gains a better “foothold”, allowing the wheel to push down.

5. IMPLICATIONS TO INFLATABLE ROBOTIC ROVER DESIGN

Inflatable wheels can achieve much larger diameters for a given mass and initial volume than their conventional counterparts. That trait makes inflatable wheels particularly attractive for robotic applications involving locomotion over extreme natural terrain. Large inflatable tires can overcome greater obstacles, thus enabling greater terrain access and reach. Moreover, the use of larger inflatable tires simplifies the navigation problem because a rover equipped with such wheels can safely and effectively surmount more and greater obstacles thus reducing the burden on the robot’s operator or the robot’s autonomous navigation system.

This research has pursued the mobility characterization of a robotic inflatable wheel through experimentation and in-depth analysis of data achieved in a specialized testbed. We experimented with 1.4 m-diameter cleated and smooth tires deployed in a variety of terrain profiles. The first significant result is that a driven lightweight inflatable wheel interacts with the terrain in a way similar to that of a very low inflation pneumatic tire (“elastic mode” tire) with the same contact patch and vertical loading. It is worth noting that a tire without internal “stiffening” structures requires far less than 0.5 psi of pressure to inflate to its maximum diameter. Therefore the tire is very compliant and conforms to the terrain quite well. That results in better traction performance but causes more tire wear.

A unique attribute of the specific inflatable wheel design (spherical shape, pass-thru axle, inner tube, no radial internal structure or spokes) is that there is significant twist in the tire about the axle attachment. The “twisting” of the tire increases its torsional rigidity to a level that the tire can react to the tangential ground loads and forward locomotion is achieved. As the wheel moves forward the tire partially “unwinds” releasing some of the elastic deformation energy into helping the forward movement. This complicated phenomenon requires further theoretical as well as experimental investigation, especially because it has an effect on the efficacy of the technique used to control the rotation of the wheel and speed of locomotion.

Another important result of this study is that closed-loop velocity control worked fairly well despite inaccuracies in the wheel model caused by the wheel diameter and contact point changing continuously. The rolling radius of the wheel literally changes instantaneously as the tire conforms to obstacles and the terrain. However these dynamics did not cause significant error with the PID velocity controller. But questions remain about how to coordinate several inflatable wheels on a multi-wheeled vehicle. Will velocity control prove capable if we close the loop by sensing motion where the wheel contacts the ground rather than with encoders at the motor output? Can

coordination be achieved with a traction controller such as that described in [8]? In the upcoming implementation we will implement and evaluate alternative control strategies such as traction/slip control and hybrid torque/velocity control.

6. ACKNOWLEDGEMENTS

This research was funded by the Jet Propulsion Laboratory. We would like to thank James Teza, Stuart Heys and David Wettergreen of Carnegie Mellon University for their valuable efforts in the development of the testbed, execution of experiments and interpretation of results.

7. REFERENCES

1. J. Jones, "Inflatable Robotics for Planetary Exploration," Proceedings of the 6th International Symposium on Artificial Intelligence, Robotics, and Automation in Space, I-SAIRAS, Montreal, Canada, June 2001.
2. J. R. Matijevic, et. al, "Characterization of the Martian Surface Deposits by the Mars Pathfinder Rover, Sojourner," Science, vol. 278, December 1997, pp. 1765-1767.
3. D. Bernard, "Preliminary Look at Hazard Models for Mars Landing," JPL Interoffice Memorandum, IOM3412-00-20, March 2000.
4. H. Moore and B. Jakosky, "Viking Landing Sites, Remote-Sensing Observations, and Physical Properties of Martian Soil Materials," Icarus, vol. 81, 1989, pp. 164-184.
5. D. Scott, "This Walking Wheel Turns Itself," Popular Science Article, July 1964, pp. 44-46.
6. D. Apostolopoulos, M.D. Wagner, S. Heys, and J. Teza, "Results of the Inflatable Robotic Rover Testbed," Technical Report CMU-RI-TR-03-18, Robotics Institute, Carnegie Mellon University, June, 2003.
7. M. Bekker, Theory of Land Locomotion, University of Michigan Press, Ann Arbor, MI, 1956.
8. K. Yoshida, T. Watanabe, N. Mizuno and G. Ishigami, "Slip, Traction Control, and Navigation of a Lunar Rover", Proceedings of the 7th International Symposium on Artificial Intelligence, Robotics and Automation in Space, NARA, Japan, May 19-23, 2003.